Thin Solid Films 518 (2010) 2134–2140

Contents lists available at ScienceDirect

Thin Solid Films

journal homepage: www.elsevier.com/locate/tsf

Reflectance of surfactant-templated mesoporous silica thin films: Simulations versus experiments

Neal J. Hutchinson [a], Thomas Coquil [a], Erik K. Richman [b], Sarah H. Tolbert [b,1], Laurent Pilon [a,*]

[a] University of California, Los Angeles, Henry Samueli School of Engineering and Applied Science, Mechanical and Aerospace Engineering Department, 420 Westwood Plaza, Los Angeles, CA 90095, USA
[b] University of California, Los Angeles, Department of Chemistry and Biochemistry, 607 Charles E. Young Drive East, Box 951569, Los Angeles, CA 90095-1569, USA

ARTICLE INFO

Available online 14 August 2009

Keywords:
Mesoporous
Nanocomposite
Optical properties
Nanophotonics
Effective medium approximation
Photocatalysis

ABSTRACT

In this study, cubic and hexagonal mesoporous amorphous silica thin films were synthesized using evaporation-induced self-assembly process followed by calcination leaving highly ordered spherical or cylindrical pores in a silica matrix. The films featured pores with diameter between 4 and 11 nm, lattice parameter from 7.8 to 24 nm, and porosity between 22% and 45%. All films were dehydrated prior to reflectance measurements except for one film which was fully hydrated. The present study compares the spectral reflectance measured experimentally between 400 and 900 nm with that computed numerically by solving three-dimensional Maxwell's equations in mesoporous silica thin films with the same morphology as those synthesized. The matrix was assumed to have the same optical properties as bulk fused silica. The pore optical properties were either those of air or liquid water whether the film was dehydrated or hydrated, respectively. Excellent agreement was found between experimental and numerical reflectance for both cubic and hexagonal mesoporous silica films. This study experimentally validates our simulation tool and offers the prospect of ab-initio design of nanocomposite materials with arbitrary optical properties without using effective medium approximation or mixing rules.

1. Introduction

Mesoporous silica has been intensively studied in the last two decades due to the simplicity of their synthesis [1] and for their numerous applications including low-k dielectrics [2–4], photocatalysis [5], optical materials [2,3,6], thermal insulation [7], optical data storage [8], corrosion-resistant catalyst supports [9], as well as drug delivery and biosensors [10–12]. Those materials can assume various shapes such as spheres, fibers, and thin-films [1]. Knowledge of their optical properties is essential for accurate design and performance optimization.

Moreover, porosity and pore size distribution of mesoporous thin films can be measured by conventional nitrogen adsorption porosimetry consisting of measuring changes in mass as N_2 adsorbs within the porous structure at cryogenic temperature. However, relatively large amount of mesoporous materials is needed and thin films must be removed from their substrates. Alternatively, porosity of mesoporous thin films can be estimated non-destructively by measuring their refraction index using ellipsometry at the typical wavelength of 632.8 nm. More recently, Baklanov et al. [13] have developed the so-called ellipsometric porosimetry [13] consisting of in situ measurements of reflectance changes, at a given wavelength, as water adsorbs and desorbs within the mesoporous thin films. This method can be used at room temperature directly on films deposited on any substrate with known optical properties, and can measure the local pore size distribution and porosity of a small sampling volume [13]. Finally, porosity can also be estimated through spectral reflectance measurements in the ultraviolet–visible part of the spectrum [14,15]. These optical techniques rely on some effective medium approximations (EMAs) relating the film's effective index of refraction and porosity.

The most commonly used EMAs are the Maxwell-Garnett theory (MGT) [16,17], Drude [18,19] (also called the Silberstein formula [17,20]), symmetric and nonsymmetric Bruggeman [17,21], Lorentz-Lorenz [18,22–25], parallel [26] (also called Birchak formula [17]) and Volume Averaging Theory (VAT) [27,28] models. Expressions for these models are summarized in Table 2. The MGT model is expressed for both 3D spherical inclusions (3D MGT) and 2D cylindrical inclusions (2D MGT) [17]. In brief, the effective properties (subscript "eff") are expressed as functions of the porosity and the properties of the continuous phase (subscript "c") and of the dispersed phase (subscript "d"). Baklanov et al.[13] and Hwang et al.[15] used the Lorentz-Lorenz model while Boissière et al.[29] and Balkenende et al.[30] used the Bruggeman model. Si et al.[31] reported that the dielectric constant $\varepsilon_r(=n_{\text{eff}}^2)$ of nanoporous SiO_2 films deposited by gas evaporation

* Corresponding author. Tel.: +1 310 206 5598; fax: +1 310 206 2302.
E-mail addresses: tolbert@chem.ucla.edu (S.H. Tolbert), pilon@seas.ucla.edu (L. Pilon).
[1] Tel.: +1 310 206 4767; fax: +1 310 206 4038.

0040-6090/$ – see front matter © 2009 Elsevier B.V. All rights reserved.
doi:10.1016/j.tsf.2009.08.006

satisfies the series model. Taylor et al.[26,32,33] used the parallel model to determine the porosity of porous silica, titania, and/or zirconia and alumino-silicate thin films made by sol–gel processes. Thus, in the previously mentioned studies, the choice of the EMA model has often been arbitrary and some experimental data sets appear to be contradictory.

Recently, Pilon and co-workers [34–37] performed detailed simulations of electromagnetic waves traveling in two- and three-dimensional non-absorbing and absorbing mesoporous thin films with various porosities as well as pore sizes, shapes, and spatial arrangements. Maxwell's equations were solved through a continuous matrix with a large number of embedded pores and accounted for boundary conditions at each interface. They showed that refraction and absorption indices of 3D cubic mesoporous thin films with spherical pores arranged in simple, body-centered (BCC), or face-centered (FCC) cubic structures were independent of polarization, pore diameter, and film morphology and depended only on porosity [37]. By contrast, optical properties of 2D hexagonal mesoporous films with cylindrical pores depended on porosity, pore shape and polarization for transverse magnetic (TM) polarized incident waves [36] but depended only on porosity for transverse electrical (TE) polarized waves [34–36]. The effective refractive and absorption indices of 3D mesoporous films showed good agreement with predictions by the 3D MGT and nonsymmetric Bruggeman EMAs, respectively [37]. Those of 2D films with cylindrical pores agreed with the VAT model [27,28] for TE polarized waves [34,35]. For TM polarized waves the effective refractive and absorption indices agreed best with predictions by the 2D MGT and parallel model [36], respectively.

This paper aims to validate this numerical simulation tool against experimental data to optically design three-dimensional heterogeneous nanostructures. First, the mesoporous thin films synthesis methods and reflectance measurement setup are described. Then, characterization of the synthesized films is presented. Finally, numerical simulation results for reflectance of mesoporous thin films, having the same morphology and thickness as those measured experimentally, are compared with experimental reflectance for dehydrated cubic and hexagonal mesoporous silica films as well as a fully hydrated cubic film.

2. Materials and methods

2.1. Material synthesis

Highly ordered cubic or hexagonal mesoporous silica thin films were synthesized based on the calcination of self-assembled surfactant micelles in an amorphous SiO_2 matrix [38]. The surfactants used were poly(ethylene oxide)-poly(propylene oxide)-poly(ethylene oxide) triblock copolymer ($EO_{20}PO_{70}EO_{20}$ or P123) and polyoxyethylene (10) stearyl ether (Brij76). Three types of films were produced namely (i) P123 cubic, (ii) P123 hexagonal, and (iii) Brij76 cubic mesoporous silica films. Synthesis of the cubic mesoporous silica thin films using Brij76 and P123 were based on methods developed by Jung and Park [39] and Alberius et al. [40], respectively. Pores in these cubic films were spherical and arranged in a FCC lattice. Similarly, hexagonal mesoporous silica thin films from P123 were synthesized following the method described by Zhao et al. [41]. They consisted of a honeycomb pattern of cylindrical pores with the unique hexagonal axis oriented parallel to the substrate.

Synthesis of the P123 cubic film was accomplished using a mixture of P123, ethanol (EtOH), 0.01 molar (M) hydrochloric acid (HCl), and tetraethyl orthosilicate (TEOS) in the by mass ratios P123:EtOH:HCl:TEOS = 0.75:8.91:2.41:4.65. First the P123 was dissolved in 3.57 g of EtOH and stirred for 30 min. Second, the HCl and TEOS were mixed with 5.36 g of EtOH and stirred for 20 min. Both solutions were combined and refrigerated for 10 min at 15 °C. The solution had to be used within the next hour for optimal results. The withdrawal rate was 2 cm/min at a stable 50% relative humidity (RH). Post processing consisted in 1 day aging at 90% RH followed by 1 day at 60 °C and calcination. Calcination was performed by heating the sample up to 450 °C with 4 h of soak time through a 1 °C/min heat ramp. The process was then completed by a 1 °C/min cool down ramp to 25 °C. The heating ramp was performed under inert nitrogen atmosphere.

Synthesis of the cubic mesoporous silica framework using Brij76 was accomplished using a mixture of Brij76, EtOH, 0.01 M HCl, and TEOS in the by mass ratios Brij76:EtOH:HCl:TEOS = 0.17:4.42:0.43:1. A silica solution was made with 0.1 g of HCl, 1 g of TEOS, and 0.84 g of EtOH. The solution was stirred in 60 °C water bath for 90 min. A polymer solution was then made with 3.58 g of EtOH, 0.34 g of 0.142 M HCl, and 0.17 g of Brij 76. Solutions were mixed and stirred for one day. Finally films were dip coated from the solution, in 25–30% RH, and withdrawn at 0.2 to 2 cm/min. Calcination followed with a heat ramp to 60 °C at 0.3 °C/min, a hold of 4 h, then another ramp to 450 °C, held also for 4 h. Process was completed by a 1 °C/min cool down ramp to 25 °C. The heating ramps were performed under inert nitrogen atmosphere.

Finally, synthesis of the P123 hexagonal mesoporous silica framework was accomplished using a mixture of P123, EtOH, 0.01 M HCl, and TEOS in the by mass ratios P123:EtOH:HCl:TEOS = 0.54:10:1.2:1.66. First the P123 was dissolved in 5 g of EtOH and stirred for 30 min. Second, the HCl and TEOS were mixed with 5.36 g of EtOH and stirred for 20 min. Both solutions were then combined and aged for 3 days at room temperature. The withdrawal rate varied from 0.2 to 2 cm/min at a stable 50% RH. Post processing consisted in 1 day of 90% room humidity aging followed by 1 day at 60 °C and calcination. Finally, the same calcination procedure as that used for the cubic mesoporous silica films was performed.

2.2. Film characterization

Each mesoporous SiO_2 films synthesized was characterized using (i) one-dimensional low angle X-ray diffraction (1D-XRD), (ii) two dimensional small angles X-ray scattering (2D-SAXS), and (iii) scanning electron microscopy (SEM) measurements. 1D-XRD measurements were performed with a Panalytical X'Pert PRO diffractometer. 2D-SAXS measurements were collected on beamline 1–4 at the Stanford Synchrotron Radiation Laboratory. SEM images were obtained using a JEOL 6700F. Fig. 1A shows typical normalized 1D-XRD intensity measurements for the P123 cubic, Brij76 cubic, and P123 hexagonal mesoporous SiO_2 films. It indicates that the films are highly ordered. Figs. 1B and 1C show typical 2D-SAXS patterns of P123 cubic and hexagonal mesoporous silica thin films. Finally, Fig. 2 shows SEM micrographs of the cubic and hexagonal mesoporous silica thin films considered. More details on films' characterization can be found elsewhere [42].

The porosity of the films consists of (i) the primary mesoporosity corresponding to the volume fraction occupied by the quasi-spherical pores and of (ii) the microporosity corresponding to the volume fraction occupied by the "necks" connecting the pores. Samples primary mesoporosity was estimated from the measured pore diameters and lattice spacings. Cubic films microporosity was estimated to be around 12% to 20% of the mesoporosity [43,44]. Hexagonal mesoporous films' microporosity, however, is expected to be much smaller since a geometric model of cylinders better captures the overall porosity. Consequently, the necks connecting the spherical pores in cubic mesoporous films were ignored in the numerical simulations. There was a ±5% uncertainty associated with the porosity measurements due to the 1 nm precision on distances measured with the SEM and the approximation in microporosity contribution.

For the P123 cubic mesoporous SiO_2 thin film, the pore diameter d was estimated to be 10 ± 1 nm and the lattice parameter d_k was 21 ±

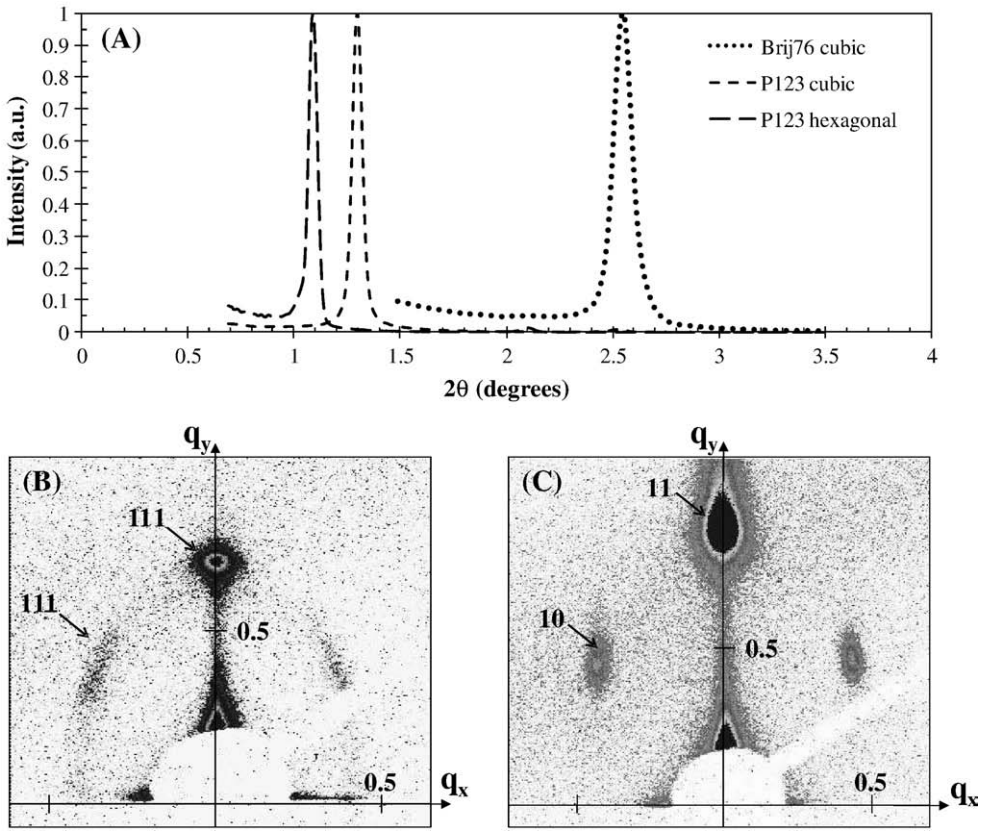

Fig. 1. (A) Normalized 1D-XRD intensity measurements for mesoporous SiO_2 thin films synthesized with P123 (cubic and hexagonal) and Brij76 (cubic). 2D-SAXS patterns of (B) a P123 cubic and, (C) a P123 hexagonal mesoporous silica thin film. Here the scattering vector q is given in nm^{-1} and defined as $q = \sqrt{q_x^2 + q_y^2} = 4\pi \sin\theta / \lambda = 2\pi / d_{spacing}$.

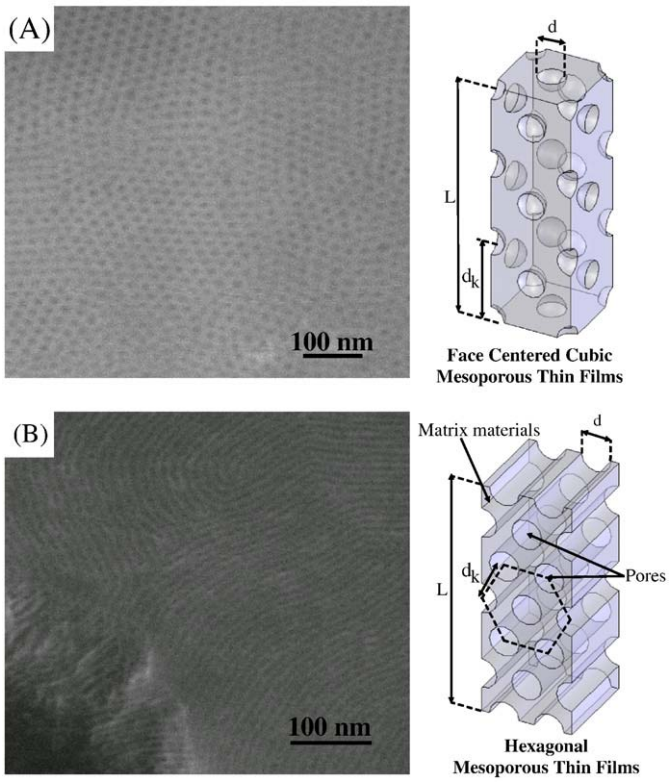

Fig. 2. SEM micrograph of P123 (A) cubic and (B) hexagonal mesoporous silica thin films (see Table 1 for dimensions).

3 nm. The porosity ϕ was calculated by considering a unit FCC cell of length d_k with spherical pores of diameter d as confirmed by 1D-XRD, 2D-SAXS, and SEM measurements. The porosity of the P123 cubic mesoporous film was then expressed as $\phi = 2\pi d^3/3d_k^3$ and equal to 22% ± 5%. Similarly, the Brij76 cubic mesoporous film featured pores 4 nm in diameter d arranged in a FCC lattice with lattice parameter d_k of 7.8 nm for an overall porosity ϕ of 29%. Results for the P123 cubic mesoporous silica film were in good agreement with those reported by Kitazawa et al.[45] for similar films and obtained using ellipsometry. On the other hand, the P123 hexagonal mesoporous thin film featured cylindrical pores 8.5 ± 1 nm in diameter d. The lattice parameter d_k was found to be 12 ± 2 nm. The porosity was estimated from $\phi = \pi d^2 / 2\sqrt{3}d_k^2$ and found equal to 45% ± 5%. These results were in good agreement with those reported by Dourdain et al.[46].

In addition, the film thickness L and the effective refraction index n_{eff} (assumed to be constant between 400 and 900 nm) were retrieved by inverse method from spectral normal reflectance measurements as described in Section 2.3. The dehydrated P123 cubic and hexagonal mesoporous films were 185 and 135 nm thick and n_{eff} was found equal to 1.34 and 1.26, respectively. The Brij76 cubic mesoporous film was 160 nm thick and its index of refraction was 1.32 and 1.44 when dehydrated or fully hydrated, respectively. The values of the film thicknesses were confirmed from the SEM images.

2.3. Normal-normal reflectance measurements

Spectral normal–normal reflectance measurements for each film were performed between 400 and 900 nm. The apparatus consisted of (i) a UV–NIR light source (Ocean optics, DH2000-BAL), (ii) a

Table 1
Characteristics of the mesoporous silica thin films synthesized and simulated.

Film	Surfactant	Pore arrangement	Pore diameter	Lattice parameter	Porosity	Refraction	Thickness
			d (nm)	d_k (nm)	ϕ	index, n_{eff}	L (nm)
1	P123	cubic (FCC)	10	21	22%	1.34[a]	185
2	P123	hexagonal	8.5	12	45%	1.26[a]	135
3	Brij76	cubic	4	7.8	29%	1.32[a], 1.44[b]	160

[a] Dehydrated.
[b] Hydrated.

bifurcated fiber (Ocean optics, R400-7-SR), (iii) a spectrometer (Ocean optics, HR4000CG UV–NIR), and (iv) a sample holder ensuring that the direction of the incident beam was normal to the sample surface. The light source was connected to the bifurcated fiber and provided polychromatic and unpolarized light. The experimental spectral reflectance of the mesoporous silica thin films was computed from,

$$R_{exp}(\lambda) = \frac{S_\lambda - D_\lambda}{M_\lambda - D_\lambda} \tag{1}$$

where S_λ was the signal reflected by the sample, D_λ is the "dark intensity", and M_λ is the reference intensity measured with a high specular reflection standard mirror (Ocean optics, STAN-SSH). The dark intensity D_λ was collected by turning off the UV–NIR light source. Before any measurements, the mesoporous cubic and hexagonal SiO_2 films were dehydrated on a hot plate for 24 hours at 160 °C to remove any traces of water which can strongly affect the reflectance measurements [47]. Then, reflectance was measured four times at room temperature immediately after being removed from the hot plate. In addition, the Brij76 cubic film was also fully hydrated under controlled relative humidity and reflectance was measured in situ.

2.4. Mesoporous thin film thickness and effective index of refraction

The effective absorption index of the mesoporous thin films was assumed to be negligibly small and set to zero over the spectral range from 400 to 900 nm as observed for dense silica glass [48,49]. In addition, scattering by the nanopores was neglected since the pore diameter (4–10 nm) was much smaller than the wavelength of the electromagnetic (EM) wave (≥400 nm) and the thin film interference effects dominate over scattering as established numerically [34–37].

The theoretical spectral normal reflectance for a homogeneous, isotropic, and non-absorbing film with uniform thickness L and optically smooth surface is expressed as [50],

$$\frac{R_{film} = r_{12}^2 + r_{23}^2 + 2r_{12}r_{23}cos(\delta_{23} - \zeta_2)}{1 + r_{12}^2 r_{23}^2 + 2r_{12}r_{23}cos(\delta_{23} - \zeta_2)} \tag{2}$$

where the Fresnel's coefficients r_{12} and r_{23}, the angle δ_{23}, and the phase difference between interfering waves ζ_2 are given by,

$$r_{12} = \frac{1 - n_{eff}}{1 + n_{eff}},\ r_{23}^2 = \frac{(n_{eff} - n_3)^2 + k_3^2}{(n_{eff} + n_3)^2 + k_3^2}, \tag{3}$$

$$\zeta_2 = \frac{4\pi n_{eff} L}{\lambda},\ \text{and}\ tan\ \delta_{23} = \frac{2n_{eff}k_3}{n_{eff}^2 - (n_3^2 + k_3^2)}$$

where n and k are the refraction and absorption indices, respectively. Subscript 3 refers to the silicon substrate while the mesoporous thin film deposited on the substrate is assumed to behave as an homogeneous medium with some effective refraction index denoted by n_{eff}.

The film thickness L and the effective refraction index n_{eff} were retrieved by inverse method using the genetic algorithm PIKAIA [51] that minimizes the root mean square of the relative error between experimental and theoretical spectral reflectance δR defined as,

$$\delta R^2 = \frac{1}{N}\sum_{i=1}^{N}\left[\frac{R_{th}(\lambda_i) - R_{exp}(\lambda_i)}{R_{exp}(\lambda_i)}\right]^2 \tag{4}$$

where $R_{exp}(\lambda_i)$ was measured at N different wavelengths λ_i between 400 and 900 nm.

2.5. Optical properties of bare silicon wafer

First, the refraction and absorption indices n_3 and k_3 of the silicon substrate, appearing in Eq. (3), were retrieved from normal-normal spectral reflectance measurements by treating the 625 μm thick polished As doped (100) silicon wafer (0.001–0.007 Ω cm) as a semi-infinite slab. Then, the normal reflectivity of the substrate were expressed as [50],

$$R_s(\lambda) = \frac{[n_3(\lambda) - 1]^2 + k_3(\lambda)^2}{[n_3(\lambda) + 1]^2 + k_3(\lambda)^2} \tag{5}$$

where n_3 and k_3 were retrieved by minimizing the root mean square of the relative error δR between $R_s(\lambda)$ and $R_{exp}(\lambda)$. The refractive index of the silicon substrate $n_3(\lambda)$ was expressed as a function of wavelength λ and temperature T as [52],

$$n_3(\lambda) = n_0(\lambda) + \gamma(\lambda)T \tag{6}$$

where $n_0(\lambda)$ and $\gamma(\lambda)$ are empirical functions. Since Jellison and Modine [52] used a lightly doped silicon wafer (doping concentration $\leq 10^{15}$ cm^{-3}), their expressions for $n_0(\lambda)$ and $\gamma(\lambda)$ could not be used for the wafer with doping concentration of 2×10^{15} cm^{-3} used in the present study. However, the same expression was used with different coefficients optimized to match the reflectance of our bare silicon wafer to yield,

$$n_0(\lambda) = \sqrt{5.609 + \frac{119.55}{3.648^2 - (1.24/\lambda)^2}} \tag{7}$$

$$\gamma(\lambda) = -2.29\times10^{-4} + \frac{6.6276\times10^{-3}}{3.648^2 - (1.24/\lambda)^2}$$

On the other hand, the absorption index $k_3(\lambda)$ reported by Jellison and Modine [52] was found to be appropriate to fit the experimental data and was expressed as,

$$k_3(\lambda) = \left\{-0.0805 + exp\left[-3.189 + \frac{7.946}{3.648^2 - (1.24/\lambda)^2}\right]\right\} \tag{8}$$

$$exp\left[\frac{T}{369.9 - \exp(-12.92 + 6.831/\lambda)}\right]$$

Note that the wavelength λ is expressed in μm and the temperature T was equal to 20 °C.

2.6. Validation

The experimental setup was validated by measuring the spectral reflectance of a 105.4 nm thick high quality thermal silicon dioxide thin film on a silicon wafer. Spectral reflectance measurements of the thermal oxide film on a Si wafer agreed well with the theoretical spectral reflectance predicted by Eqs. (2) and (3) using the Sellmeier equation for silica glass given by Malitson [48],

$$n^2_{SiO_2}(\lambda) = 1 + \frac{0.6961663\lambda^2}{\lambda^2 - (0.0684043)^2} + \frac{0.4079426\lambda^2}{\lambda^2 - (0.1162414)^2} + \frac{0.8974794\lambda^2}{\lambda^2 - (9.896161)^2} \quad (9)$$

where λ is expressed in μm. This establishes that reflectance measurements are properly performed.

2.7. Reflectance simulations

Simulations of EM wave transport through the heterogenous thin films were performed by numerically solving the three-dimensional Maxwell's equations along with the associated boundary conditions. The governing equations and the method of solution have been presented elsewhere and need not be repeated [36]. The morphologies of the cubic and hexagonal mesoporous thin films simulated and the coordinate system are reproduced in Fig. 3. The pore diameter d, lattice parameter d_k, porosity ϕ, and film thickness L measured experimentally were used in establishing the dimensions of the numerical models.

Simulations were performed at 10 to 40 wavelengths between 400 and 900 nm. Other input parameters included (i) the spectral refraction and absorption indices of the silicon substrate $n_3(\lambda)$ and $k_3(\lambda)$ given by Equations (6) and (8) and (ii) the refractive index n_{SiO2} of the matrix in cubic and hexagonal mesoporous silica thin films given by Eq. (9). For each wavelength, Maxwell's equations were solved in the frequency domain using COMSOL Multiphysics 3.4 applying the Galerkin finite element method on unstructured meshes and using parallel computing on a Dell Precision 690 with two 2.33 GHz Quad-Core Intel Xeon CPU and 24 GB of RAM. The local instantaneous electric and magnetic field vectors, denoted by $\vec{E}$ and $\vec{H}$ and solutions of Maxwell's equations, were computed throughout the 3D heterogeneous nanostructures. Then, the mesoporous thin films' reflectance was estimated as the ratio of the norm of the time- and area-averaged reflected and incident Poynting vectors, i.e., $R_{num}(\lambda) = |\Pi_{x,r}|_{avg}/|\Pi_{x,0}|_{avg}$ where $|\Pi_{x,0}|$ and $|\Pi_{x,r}|$ are the x-component of the local time-averaged incident and reflected Poynting vectors defined as $|\vec{\Pi}| = Re\{E \times \vec{H}^*\}/2$. They have been further averaged over the top surface of the mesoporous films as referred by subscript "avg". The incident Poynting vector was normal to and uniform over the film surface. For hexagonal mesoporous films, polarization of the incident EM wave affects the reflectance [36]. Here, TE and TM polarizations are defined such that the incident electric and magnetic field vectors are parallel to the cylindrical pores main axis, respectively. In other words, the incident electric field vector is such that $\vec{E}_0 = E_0\vec{e}_z$ for TE polarization and $\vec{E}_0 = E_0\vec{e}_y$ for TM polarization as illustrated in Fig. 3. By contrast, polarization of the incident EM wave has no effect on reflectance of cubic mesoporous films due to their symmetric morphology [37].

3. Results and discussion

3.1. Comparison between experimental and numerical reflectance

First, care was taken to ensure that all numerical results reported were numerically converged, i.e., they were independent of the number and size of the finite element meshes. A total of 65,310 and 16,472 tetrahedral elements were necessary to obtained a converged solution for cubic and hexagonal mesoporous films, respectively. It was also verified that the reflected time-averaged Poynting vector $\vec{\Pi}_r$ was normal to and nearly uniform over the film surface. The relative difference between the norms of the local time-averaged $|\vec{\Pi}_r|$ and the time- and area-averaged $|\vec{\Pi}_r|_{avg}$ Poynting vectors at the air-film interface was less than 1.12% and 0.05% for the cubic and hexagonal mesoporous thin films, respectively.

3.1.1. P123 Cubic mesoporous film

Fig. 4 compares the experimentally measured reflectance $R_{exp}(\lambda)$ for the dehydrated P123 cubic film and the associated theoretical

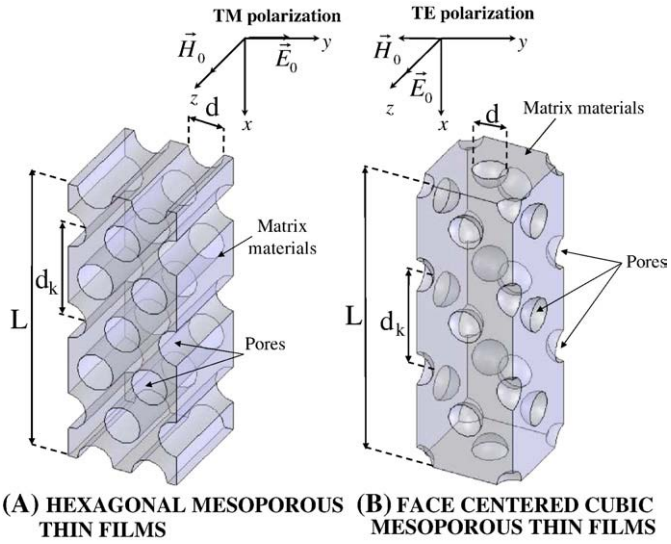

Fig. 3. Schematic of numerically simulated (A) hexagonal and (B) cubic mesoporous silica films with the same morphology as those synthesized by evaporation-induced self-assembly along with coordinate system.

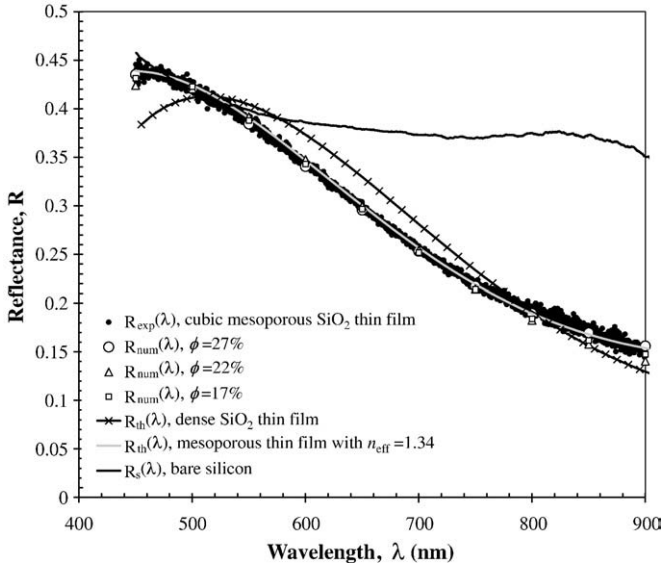

Fig. 4. Experimental spectral reflectance of a silicon substrate bare and coated with a 185 nm thick P123 cubic mesoporous silica thin film (L = 185 nm, d = 10 nm, d_k = 21 nm, and ϕ = 22%) along with computed numerical predictions and theoretical reflectance of a dense SiO_2 thin film of identical thickness and porosity ϕ = 17%, 22%, and 27%.

reflectance $R_{th}(\lambda)$ given by Eq. (2) estimated with the values of $L=185$ nm and $n_{eff}=1.34$ retrieved by inverse method. Excellent agreement was observed between $R_{exp}(\lambda)$ and $R_{th}(\lambda)$ giving confidence in the retrieved values of L and n_{eff} considering how sensitive $R_{th}(\lambda)$ is to both parameters.

Fig. 4 also shows the numerically computed spectral reflectance $R_{num}(\lambda)$ of P123 cubic mesoporous thin films with three different porosities within the experimental uncertainty namely 17%, 22%, and 27% achieved numerically with pore diameter equal to 9.2, 10, and 10.7 nm, respectively while lattice parameter remained the same. The numerical predictions were in very good agreement with experimental measurements. Indeed, the experimental reflectance falls within numerical predictions for porosities 17%, 22%, and 27%. Moreover, Fig. 4 shows the theoretical reflectance of a dense silica film ($\phi=0\%$) of identical thickness. Changes in reflectance is appreciable when porosity varies from 0% to 22% but is not significant for porosities within the experimental uncertainty. These results indicate that (i) the silica matrix has the same optical properties as bulk silica [48,49], (ii) absorption by the silica matrix can safely be neglected and (ii) the porosity can be reasonably estimated from SEM, 1D-XRD, 2D-SAXS measurements and geometry consideration.

3.1.2. P123 Hexagonal mesoporous film

Similarly, Fig. 5 shows the spectral reflectance obtained experimentally and that numerically computed for TE and TM polarizations for the dehydrated P123 hexagonal film. It is evident that the experimentally measured reflectance falls between the numerical reflectance for TE and TM waves over most of the spectrum considered. Indeed, experimentally, the light traveling through the bifurcated fiber is unpolarized and corresponds to the arithmetic mean of reflectances for TE and TM polarizations. The minor discrepancies could be attributed to the experimental uncertainty in the porosity or in the substrate's optical properties (n_3 and k_3) whose effect is important since the film was very thin.

Fig. 5 also shows the theoretical reflectance of a dense SiO_2 film having the same thickness as that experimentally measured for the dehydrated mesoporous films considered. For both dehydrated cubic and hexagonal mesoporous films, it is evident that the presence of the pores in the silica matrix significantly affects the film spectral reflectance.

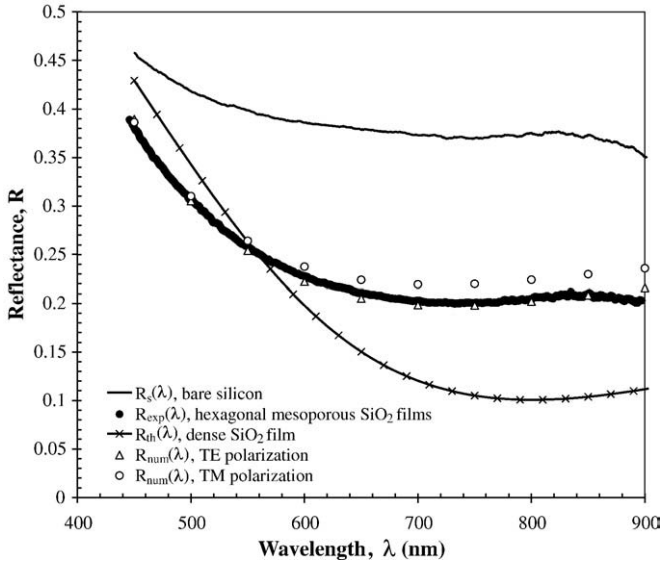

Fig. 5. Experimental spectral reflectance of a bare silicon substrate and one coated with a 135 nm thick P123 hexagonal mesoporous silica thin film ($L=135$ nm, $d=8.5$ nm, $d_k=12$ nm, and $\phi=45\%$) along with computed numerical predictions for TE and TM polarization and theoretical reflectance of a dense SiO_2 thin film of identical thickness.

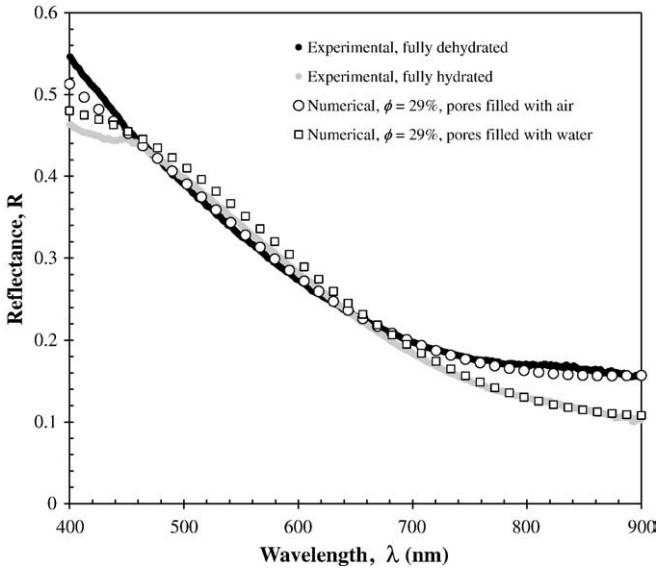

Fig. 6. Experimental spectral reflectance of a fully dehydrated (RH <10%) and fully hydrated (RH >35%) Brij 76 cubic mesoporous silica thin film ($L=160$ nm, $d=4$ nm, $d_k=7.8$ nm, and $\phi=29\%$) along with computed numerical predictions.

3.1.3. Dehydrated and hydrated Brij76 cubic mesoporous film

It has been established that water interfaces with large radius of curvature or confined water droplets feature density, hydrogen bond network, and surface tension different from bulk properties [29]. It remains unclear, however, how this affects the optical properties of a confined water "droplet". A Brij76 cubic mesoporous film was chosen for its small pores in which capillary condensation take place more easily than in larger pores. The film was dehydrated on a hot plate at 160 °C for more than 24 hours before cooling at room temperature and performing reflectance measurements. In addition, the film was fully hydrated by placing it for several hours in RH in excess of 35% before measuring the reflectance in situ. Increasing the RH further did not affect reflectance suggesting that the film was saturated. The fully hydrated film was simulated as previously described by assuming the pores to be filled with liquid water whose optical properties were assumed to be the same as those of bulk liquid water reported by Hale and Querry [53].

Fig. 6 shows the experimentally measured and numerically predicted reflectance of a 160 nm thick fully dehydrated and hydrated Brij76 cubic mesoporous thin film. It clearly illustrates the effect of film hydration on its spectral reflectance. Very good agreement was found between experimentally measured and numerically simulated reflectances for both dehydrated and fully hydrated cases. This suggests that water confined in the pores optically behaved like liquid water.

4. Discussion

Using the different EMAs whose expressions are provided in Table 2 for the value of $n_2=1.34$ for P123 cubic mesoporous silica film of porosity 22%±5% and assuming the SiO_2 matrix has a refraction index equal to 1.457 at 632.8 nm [49], the retrieved porosity was found equal to 25% (3D MGT), 25% (symmetric Bruggeman), 23% (Lorentz–Lorenz), 29% (Drude), 25% (parallel), and 29% (VAT). Similarly, for the P123 hexagonal mesoporous film with 45% porosity, the retrieved index of refraction was found to be $n_{eff}=1.26$ and the porosity was found to be 40% (2D MGT), 42% (symmetric Bruggeman), 40% (Lorentz–Lorenz), 48% (Drude), 43% (parallel), and 48% (VAT).

Porosity predictions by the different EMAs are similar for mesoporous SiO_2 and predicts porosity within the experimental uncertainty. However, the differences between one EMA and another can be significant and increase as the index of refraction of the matrix

Table 2
Expressions of different effective medium approximations (EMAs) widely used in the literature.

0.8		
EMA model	Formula	Ref.
3D Maxwell-Garnett Theory (3D MGT)	$n_{\text{eff}}^2 = n_c^2\left[1-\frac{3\phi(n_c^2 n_d^2)}{2n_c^2+n_d^2+\phi(n_c^2-n_d^2)}\right]$	[16]
2D Maxwell-Garnett Theory (2D MGT)	$n_{\text{eff}}^2 = n_c^2\left[1-\frac{2\phi(n_c^2-n_d^2)}{n_c^2+n_d^2+\phi(n_c^2-n_d^2)}\right]$	[17]
Drude (or Silberstein)	$n_{eff}^2=(1-\phi)n_c^2+\phi n_d^2$	[18,19]
Symmetric Bruggeman	$(1-\phi)\frac{n_c^2-n_{eff}^2}{n_c^2+2n_{eff}^2}+\phi\frac{n_d^2-n_{eff}^2}{n_d^2+2n_{eff}^2}=0$	[17,21]
Nonsymmetric Bruggeman	$1-\phi=\frac{\left(\frac{n_{\text{eff}}^2}{n_c^2}-\frac{n_d^2}{n_c^2}\right)}{\left[\left(\frac{n_{\text{eff}}^2}{n_c^2}\right)^{1/3}\left(1-\frac{n_d^2}{n_c^2}\right)\right]}$	[17]
Lorentz–Lorenz	$\frac{n_{\text{eff}}^2-1}{n_{\text{eff}}^2+2}=(1-\phi)\left(\frac{n_c^2-1}{n_c^2+2}\right)+\phi\left(\frac{n_d^2-1}{n_d^2+2}\right)$ $A=\phi(n_d^2-k_d^2)+(1-\phi)(n_c^2-k_c^2)$ $B=2n_dk_d\phi+2n_ck_c(1-\phi)$	[22,24,25]
Volume Averaging Theory (VAT)	$n_{\text{eff}}^2=\frac{1}{2}[A+\sqrt{A^2+B^2}]$ $k_{\text{eff}}^2=\frac{1}{2}[-A+\sqrt{A^2+B^2}]$	[27,28]
Parallel (or Birchak)	$n_{\text{eff}}=(1-\phi)n_c+\phi n_d$	[17]

increases [34]. Alternatively, the porosity can be retrieved from spectral reflectance measurements without relying on some effective medium approximation selected arbitrarily and potentially giving a wide range of porosity for the same effective index of refraction. This is particularly true for mesoporous or nanocomposite materials with large mismatch in index of refraction between the continuous and disperse phases.

5. Conclusion

This paper presented detailed numerical simulations and experimental measurements of spectral reflectance of cubic and hexagonal mesoporous silica thin films between 400 and 900 nm. The films were synthesized by evaporation induced self-assembly followed by calcination of surfactant micelles. Films were characterized using 1D-XRD, 2D-SAXS, and SEM measurements as well as reflectance measurements. The 3D numerical simulations accurately modeled the morphology of the films investigated using the pores' spatial arrangement and diameter, lattice parameter, and porosity measured experimentally. The results suggests that silica matrix had the same index of refraction as bulk silica glass (amorphous) [48]. Excellent agreement was found between numerical predictions and experimentally measured reflectance for both P123 cubic and hexagonal mesoporous thin films and the dehydrated or hydrated Brij76 cubic film. In addition, when the film was fully hydrated, the phase occupying the pores had the same index of refraction as liquid water. This study also validates experimentally the numerical tool and the numerical results reported in our previous studies [34–37]. The method and the results can be used to design and guide the synthesis of nanostructures with desired optical properties for various applications without relying on EMAs or mixing rules.

Acknowledgement

The authors thank Thomas Quickel for the 2D-SAXS measurements. This material is based upon work supported by the National Science Foundation under Grants CTS 0449429 (L.P.) and CHE-0527015(S.H.T) and by Intel, NERC and UC Discovery Program. Portions of this research were carried out at the Stanford Synchrotron Radiation Laboratory, a national user facility operated by Stanford University on behalf of the U.S. Department of Energy, Office of Basis Energy Science.

References

[1] C. Brinker, Y. Lu, A. Sellinger, H. Fan, Adv. Mater. 11 (7) (1999) 579.
[2] G. Wirnsberger, P. Yang, B. Scott, B. Chmelka, G. Stucky, Spectrochim. Acta Part A 57 (2001) 2049.
[3] A. Jain, S. Rogojevic, S. Ponoth, N. Agarwal, I. Matthew, W. Gill, P. Persans, M. Tomozawa, J. Plawsky, E. Simonyi, Thin Solid Films 398–399 (1) (2001) 513.
[4] E. Kondoh, M. Baklanov, E. Lin, D. Gidley, A. Nakashima, Jpn J. Appl. Phys. 40 (2001) L323.
[5] D. Shcukin, D. Sviridov, J. Photochem. Photobiol. C 7 (1) (2006) 23.
[6] A. Péard, T. Gacoin, J.-P. Boilot, Acc. Chem. Res. 40 (9) (2007) 895.
[7] S. Choi, T.-J. Ha, B.-G. Yu, S. Jaung, O.K. Tan, H.-H. Park, Ceram. Int. 34 (4) (2008) 833.
[8] J. Wang, G. Stucky, Adv. Funct. Mater. 14 (5) (2004) 409.
[9] Q. Hu, R. Kou, J. Pang, T. Ward, M. Cai, S. Yang, Y. Lu, J. Tang, Chem. Commun. 6 (2007) 601.
[10] B.G. Trewyn, S. Giri, I. Slowing, V.S.-Y. Lin, Chem. Commun. 31 (2007) 3236.
[11] M. Arroyo-Hernandez, R. Martin-Palma, J. Perez-Rigueiro, J. Garcia-Ruiz, J. Garcia-Fierro, J.M. Martinez-Duart, Mater. Sci. Eng. C 23 (6–8) (2003) 697.
[12] R. Martin-Palma, V. Torres-Costa, M. Arroyo-Hernandez, M. Manso, J. Perrez-Rigueiro, J. Martinez-Duart, Microelectron. J. 35 (1) (2004) 45.
[13] M. Baklanov, K. Mogilnikov, V. Polovinkin, F. Dultsev, J. Vac. Sci. Technol., B, Microelectron. Nanometer Struct. 18 (3) (2000) 1385.
[14] V.A. Sterligov, Appl. Opt. 44 (21) (2005) 4538.
[15] Y. Hwang, K. Patil, S. Jhung, J.-S. Chang, Y. Ko, S.-E. Park, Microporous Mesoporous Mater. 78 (2–3) (2005) 245.
[16] J.C.M. Garnett, Philos. Trans.-R. Soc. Lond. Series A 203 (359–371) (1904) 385.
[17] A. Sihvola, IEE electromagnetic waves series 47, The Institution of Electrical Engineers, London, UK, 1999.
[18] N. Sahoo, S. Thakur, R. Tokas, N. Kamble, Appl. Surf. Sci. 253 (16) (2007) 6787.
[19] C.-C. Lee, C.-J. Tang, Appl. Opt. 45 (36) (2006) 9125.
[20] L. Silberstein, Ann. Phys. und Chemie, Leipzig, 1895, p. 661.
[21] D. Bruggeman, Ann. Phys. 416 (7 and 8) (1935) 636–664 and 665.
[22] D. Aspnes, American Journal of Physics 50 (8) (1982) 704.
[23] S. Bosch, J. Ferr-Borrull, J. Sancho-Parramon, Solid-State Electron. 45 (5) (2001) 703.
[24] L. Lorenz, Ann. Phys. und Chemie 247 (9) (1880) 70.
[25] H. Lorentz, Ann. Phys. und Chemie 245 (4) (1880) 641.
[26] D. Taylor, P. Fleig, S. Hietala, Thin Solid Films 332 (1–2) (1998) 257.
[27] J. del Rio, S. Whitaker, Transp. Porous Media 39 (2) (2000) 159.
[28] J. del Rio, S. Whitaker, Transp. Porous Media 39 (3) (2000) 259.
[29] C. Boissière, D. Grosso, S. Lepoutre, L. Nicole, A. Bruneau Brunet, C. Sanchez, Langmuir 21 (26) (2005) 12362.
[30] A. Balkenende, F. de Theije, J. Kriege, Adv. Mater. 15 (2) (2003) 139.
[31] J. Si, H. Ono, K. Uchida, S. Nozaki, H. Morisaki, N. Itoh, Appl. Phys. Lett. 79 (19) (2001) 3140.
[32] A. Jain, S. Rogojevic, S. Ponoth, W. Gill, J. Plawsky, J. Appl. Phys. 91 (5) (2002) 3275.
[33] B.-Y. Tsui, C.-C. Yang, K.-L. Fang, IEEE Transactions on Electron Devices 51 (1) (2004) 20.
[34] M. Braun, L. Pilon, Thin Solid Films 496 (2) (2006) 505.
[35] A. Garahan, L. Pilon, J. Yin, I. Saxena, J. Appl. Phys. 101 (1) (2007) 014320.
[36] A. Navid, L. Pilon, Thin Solid Films 516 (12) (2008) 4159.
[37] N. Hutchinson, T. Coquil, A. Navid, L. Pilon, Thin Solid Films (in press).
[38] B. Eggiman, M. Tate, H. Hillhouse, Chem. Mater. 18 (3) (2006) 723.
[39] S. Jung, H. Park, Thin Solid Films 494 (1–2) (2006) 320.
[40] P. Alberius, K. Frindell, R. Hayward, E. Kramer, G. Stucky, B. Chmelka, Chem. Mater. 14 (8) (2002) 3284.
[41] D. Zhao, P. Yang, D. Margolese, B. Chmelka, G. Stucky, Chem. Commun. 22 (1998) 2499.
[42] T. Coquil, E. Richman, N. Hutchinson, S. Tolbert, L. Pilon, J. Appl. Phys. 106 (3) (2009) 034910.
[43] D. Fattakhova-Rohlfing, M. Wark, T. Brezesinski, B. Smarsly, J. Rathousk, Adv. Funct. Mater. 17 (1) (2007) 123.
[44] B. Smarsly, C. Goltner, M. Antonietti, W. Ruland, E. Hoinkis, J. Phys. Chem. B 105 (4) (2001) 831.
[45] N. Kitazawa, H. Namba, M. Aono, Y. Watanabe, J. Non-Cryst. Solids 332 (1–3) (2003) 199.
[46] S. Dourdain, A. Mehdi, J. Bardeau, A. Gibaud, Thin Solid Films 495 (1–2) (2006) 205.
[47] M.C. Fuertes, S. Colodrero, G. Lozano, A.R. Gonzalez-Elipe, D. Grosso, C. Boissiere, C. Sanchez, G.J.d.A.A. Soler-Illia, H. Miguez, J. Phys. Chem. C 9 (2008) 3157.
[48] I. Malitson, J. Opt. Soc. Am. 55 (10) (1965) 1205.
[49] R. Kitamura, L. Pilon, M. Jonasz, Appl. Opt. 46 (33) (2007) 8118.
[50] M.F. Modest, Radiative Heat Transfer, Academic Press, San Diego, CA, 2003.
[51] P. Charbonneau, B. Knapp, PIKAIA, High Altitude Observatory, National Center for Atmospheric Research, Boulder, CO., 2002. URL http://www.hao.ucar.edu/Public/models/pikaia/pikaia.html.
[52] G. Jellison, F. Modine, J. Appl. Phys. 76 (6) (1994) 3758.
[53] G. Hale, M. Querry, Appl. Opt. 12 (3) (1973) 555.